Electric-field switching of the antiferromagnetic topological state in a multiferroic heterobilayer

Xilong Xu, Ting Zhang, Ying Dai,* Baibiao Huang, and Yandong Ma†
School of Physics, State Key Laboratory of Crystal Materials, Shandong University, Shandanan Street 27, Jinan 250100, China

(Received 12 May 2022; accepted 10 November 2022; published 28 November 2022)

Coupling nontrivial topological physics to ferroelectricity in two-dimensional lattice is highly desirable in both fundamental research and devices applications. Here, using first-principles calculations, we report that in a multiferroic heterobilayer consisting of a antiferromagnetic layer MnSe and a ferroelectric layer In_2S_3, the typical type-III band alignment can be realized. Upon introduction of spin-orbit coupling, a band gap is created, giving rise to a nontrivial antiferromagnetic topological phase. By reversing ferroelectric polarization, the nontrivial antiferromagnetic topology of $MnSe/In_2S_3$ can be annihilated, yielding a wide-gap antiferromagnetic semiconductor with trivial physics. It thus proves to be a feasible approach to realize purely electric-field control of antiferromagnetic topological physics in this heterobilayer. The physical mechanism of such phenomenon is further unveiled to be related to the interlayer charge transfer between the two layers. These findings shed light on the design and control of antiferromagnetic topological physics in two dimensions.

DOI: 10.1103/PhysRevB.106.205307

Topological insulator (TI) is a new quantum state of matter with a nontrivial property. The defining signature of this novel electric state is the existence of gapless edge states within the bulk band gap. Since the first proposal of quantum spin Hall effect in graphene [1–6], it has attracted great attention and spurred rapid development due to its scientific importance and a variety of exotic characteristics, such as topological protection from disorders and defects, the high carrier mobility, and exotic optical properties [3,5,7–15]. These intriguing features not only provide unprecedented opportunities for studying nontrivial topological physics, but also hold great potential for technological application in spintronics [16–22]. In view of achieving TI-based spintronic devices with superior performance and high integration level, it is critical to realize effective control of topological properties, especially the creation and annihilation [23].

Among numerous possible strategies, ferroelectrics receives special attention. Ferroelectrics refers to the electrically switchable order of electric polarizations that forms spontaneously, and thus possesses two equivalent stable states. In ferroelectrics, the polarization is equivalent to the external electric field, but superior to electric field; it is nonvolatile and can avoid energy consumption caused by sustained electric field [24–29]. Owning to these compelling features, ferroelectric (FE) control of physical properties has been intensively investigated [30,31], particularly after the identification of ferroelectrics in two-dimensional (2D) lattices [32–35]. In fact, recent studies have shown that FE polarization can be integrated into the topological systems to realize nonvolatile control in Sb/In_2Se_3 and Bi/In_2Se_3 heterobilayers, etc. [36–39]. It suggests that the nontrivial topological state can be controlled directly by electric field through polarization switching. Nonetheless, these few existing works in this field are exclusively focused on nonmagnetic topological materials. Actually, up to now, whether such type of control can be extended to antiferromagnetic (AFM) topological states has not yet been explored.

In this work, we propose a mechanism for realizing such ferroelectric control of AFM topological state on the basis of a heterobilayer consisting of an AFM layer of MnSe and a ferroelectric layer of In_2S_3. Our first-principles calculations show that the typical type-III band alignment can be formed for the band edges of these two layers in the absence of spin-orbit coupling (SOC), leading to the metallic nature for $MnSe/In_2S_3$ heterobilayer. With including SOC, a band gap opens, suggesting the AFM topological phase for $MnSe/In_2S_3$ heterobilayer. When reversing the electric polarization through ferroelectric switching, the $MnSe/In_2S_3$ heterobilayer exhibits a wide band gap, suggesting a nontrivial-to-trivial phase transition. Evidently, the AFM topological phase in this heterobilayer can be created and annihilated by ferroelectricity. The underlying physics is discussed in detail. Our works pave a way for future devices based on AFM TIs.

Our first-principles calculations based on density-functional theory (DFT) are performed using the Vienna *Ab initio* Simulation Package (VASP) [40]. The exchange-correlation interaction is treated by the generalized gradient approximation parametrized by Perdew, Burke, and Ernzerhof [41,42]. The ion-electron interaction is treated by projector augmented-wave method. The Heyd-Scuseria-Ernzerhof (06) (HSE06) functional is employed to obtain the accurate band structures. The Monkhorst-Pack k mesh is set to $11 \times 11 \times 1$. The kinetic cutoff energy is set to 450 eV. All structures are fully relaxed until the force on each atom less than 0.01 eV/Å. The electronic iteration convergence criterion is set to 1×10^{-5} eV. To avoid spurious interactions between periodic images, a vacuum space of at least 15 Å is introduced. The

*daiy60@sina.com
†yandong.ma@sdu.edu.cn

 ©2022 American Physical Society

Wannier Charge Center and edge states of this system are calculated using the maximally localized Wannier function (MLWF) method implemented in WANNIER90 pack [43]. The DFT-D3 method is employed for treating van der Waals interaction in all calculations [44]. The ferroelectric transition pathway and energy barrier are calculated on the basis of the nudged elastic band (NEB) method [45]. Dipole moment correction is employed in all the calculations [46].

Figure S1 presents the crystal structure of single-layer (SL) MnSe, which was recently synthesized in experiment [47]. It exhibits a buckled structure with the space group of P-3m1. Each Mn atom carries a magnetic moment of 5 μ_B, and the exchange interaction among them favors a Néel-type AFM state. The band structures of SL MnSe with considering SOC are shown in Fig. S1 [48]. Clearly, SL MnSe is a semiconductor with an indirect band gap of 2.53 eV. Its conduction-band minimum (CBM) locates at the M point, while the valence-band maximum (VBM) lies at the Γ point. Because of the AFM exchange interaction, the bands are spin degenerate. Here, we select SL In_2S_3, which has been intensively investigated previously as a typical 2D FE crystal, as the FE candidate following the two reasons: (i) it has a small lattice mismatch with SL MnSe (3.4%), which can generate small unit cells for calculations; (ii) it has a suitable position of band edges that can form type-III and type-II band alignments with SL MnSe, which will be discussed in the following. SL In_2S_3 possesses an out-of-plane polarization of $1.02 \times 10^3\,\mathrm{C\,m^{-2}}$, The band structures of SL In_2S_3 is shown in Fig. S2 [48]. It displays a semiconducting behavior with a direct band gap of 1.98 eV, wherein its CBM locates at the Γ point and the VBM also lies at the Γ point.

Given the bistable FE states of In_2S_3, there are two types of MnSe/In_2S_3 heterobilayers: one with polarization pointing away from the interface ($P\downarrow$), and another with polarization pointing to the interface ($P\uparrow$). The crystal structures of $P\downarrow$ and $P\uparrow$ are displayed in Figs. 1(a) and 1(b), respectively. The optimized interlayer distances between the two ingredients are 3.897 and 3.958 Å, respectively. Each unit cell of the heterostructure contains three S, two In, two Mn, and two Se atoms. To confirm their stabilities, we calculate the adhesion energy, which is defined as $E_b = E_{total} - E_{In_2S_3} - E_{MnSe}$, where E_{total}, $E_{In_2S_3}$, and E_{MnSe} are the total energy of the heterobilayer, SL In_2S_3, and SL MnSe, respectively. For $P\downarrow$ and $P\uparrow$, the E_b are found to be 168 and 134 meV per unit cell, respectively. Such large differences in interlayer distance and E_b indicate that the interactions between MnSe and In_2S_3 are distinct between $P\downarrow$ and $P\uparrow$. This would result in significant difference in their band structures, which will be discussed below.

The absolute positions of band edges for these two materials with respect to vacuum level are shown in Fig. S3 [48]. Obviously, a typical type-III band alignment forms for $P\downarrow$. Here, we also employ the HSE06 method to calculate the positions of band edges for comparison and find the type-III band alignment remains unchanged in Supplemental Material (Fig. S3) [48] (see, also, Refs. [49–54] therein). The type-III band alignment can form band crossing between the two layers of materials, wherein a band gap may open upon including SOC. Such scenario usually implies a nontrivial phase. Different from $P\downarrow$, $P\uparrow$ would feature a type-II band alignment between

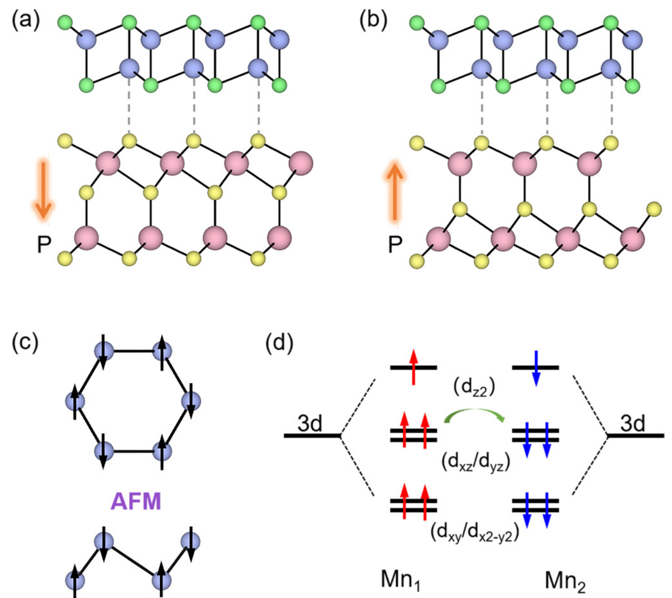

FIG. 1. Crystal structure of MnSe/In_2S_3 heterobilayer under $P\downarrow$ (a) and $P\uparrow$ (b). Purple, green, red, and yellow spheres represent Mn, Se, In, and S atoms, respectively. (c) AFM magnetic configurations in the Mn hexagonal lattice. (d) Splitting of Mn-d orbitals and the magnetic exchange coupling between adjacent Mn atoms.

the band edges of SL In_2S_3 and MnSe. Figures 2(a) and 2(e) show the charge-density difference between the two layers for MnSe/In_2S_3 heterobilayer. Here, yellow and blue colors represent electron gain and loss regions, respectively. It can be seen clearly that for $P\downarrow$, a significant electron transfer occurs between MnSe and In_2S_3 layers [Fig. 2(a)], implying the type-III band alignment, while for $P\uparrow$, the charge densities are mainly localized in the space between the two layers, suggesting no charge transfer between them, which corresponds to the type-II band alignment. Moreover, as there is no charge transfer between the two layers, the interlayer coupling for $P\uparrow$ would be weaker as compared with the case of $P\downarrow$. With these results in hand, we can also understand the difference in interlayer distance and E_b between $P\downarrow$ and $P\uparrow$.

Figure 2(b) presents the band structure of $P\downarrow$ in the absence of SOC. Due to the interlayer interaction, there is a net magnetic moment of 0.2 μ_B per unit cell. As a result, the spin degeneracy for $P\downarrow$ is split slightly, resulting in nonsymmetry for the spin-up and spin-down bands; see Fig. 2(b). We can observe that the CBM from In_2S_3 layer shifts below the Fermi level, while the VBM from MnSe layer shifts above the Fermi level; see Fig. 2(c). For more detail, as illustrated in Fig. 2(d), the CBM from In_2S_3 layer is formed by the spin-down state, which is mainly contributed by In/S-s/p_z orbitals, while for the VBM from MnSe layer, it is formed by the spin-up state, dominated by Mn-$d_{xy}/d_{x2\text{-}y2}$ and Se-p_x/p_y orbitals. This firmly confirms that the typical type-III band alignment is formed in $P\downarrow$, wherein the VBM of a material crosses the CBM of another material. Upon including SOC, as shown in Fig. 2(c), a band gap of 18 meV opens at the Dirac cone, giving rise to a semiconducting character. From Fig. 2(d), we can see that including of SOC shifts the $|In_2S_3\,\mathrm{up}\rangle$ and $|\mathrm{MnSe\,down}\rangle$ bands below and above the Fermi level,

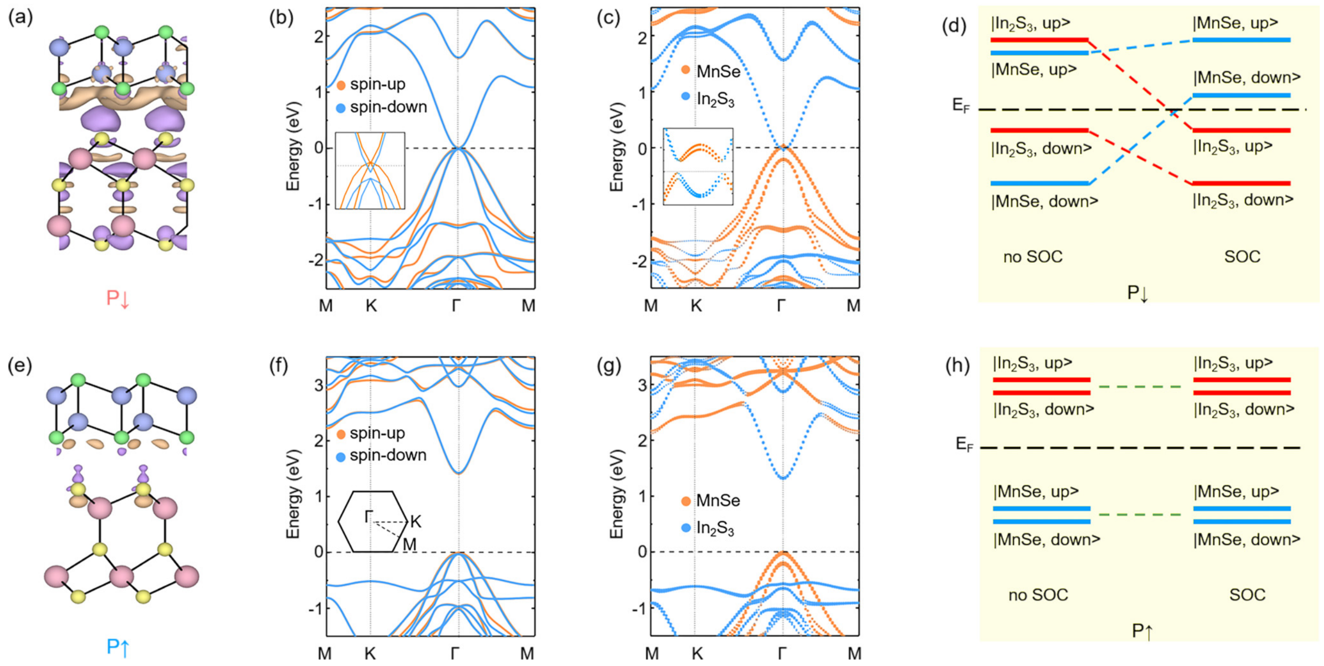

FIG. 2. Charge-density difference of $MnSe/In_2S_3$ heterobilayer under (a) $P\downarrow$ and (e) $P\uparrow$. The isosurface value is set to 0.2 electrons per Å^3. Band structures of $MnSe/In_2S_3$ heterobilayer under $P\downarrow$ without (b) and with (c) SOC, and under $P\uparrow$ without (f) and with (g) SOC. Inset in (f) shows the 2D Brillouin zone. The Fermi level is set to 0 eV. Schematic diagram of the band evolutions at Γ point for (d) $P\downarrow$ and (h) $P\uparrow$. In (d) and (h), red and blue bands correspond to the CBM and VBM of the constituent layers.

respectively. Such band order implies the nontrivial band topology in $P\downarrow$.

To estimate the nontrivial band topology in $P\downarrow$, we first calculate the topological invariant Z_2 using the Wilson loop method [55], which tracks the evolution of the Wannier center for the valence band. When the Wannier Charge Center (WCC) is crossed by any arbitrary horizontal reference lines an "odd" number of times, the system is topological nontrivial with $Z_2 = 1$. Figure 3(b) shows the evolution of WCC for $P\downarrow$. Obviously, the number of crossings between the WCC and the reference horizontal line is odd, yielding a nontrivial topological invariant $Z_2 = 1$. By considering the AFM nature of this system, we also calculate its Chern number. Intriguingly, the Chern number is estimated to be 0 for $P\downarrow$, suggesting that the nontrivial phase is quantum spin Hall (QSH) state. The hallmark of a QSH insulator is the existence of a pair of topologically protected conducting edge states in the bulk band gap. Using the MLWFs, the edge Green function of the semi-infinite lattice of $P\downarrow$ is constructed and the local density of state of the edge is shown in Fig. 3(a). We can see that within the energy window of SOC gap, a pair of gapless edge states are present for $P\downarrow$, confirming the QSH phase. It is worthy emphasizing that unlike the previously reported 2D TIs or 2D antiferromagnetic TIs [56], the intersection of these two edge states does not fall on the Γ point, but presents an asymmetric shape. This feature could be attributed to its small net magnetic moment. Therefore, we confirm that $P\downarrow$ is a 2D AFM TI.

Figure 2(f) displays the band structure of $P\uparrow$ without considering SOC. Different from the case of $P\downarrow$, due to the weak interlayer interaction, there is only a small net magnetic moment of 0.001 μ_B per unit cell. In this regard, the spin degeneracy for the bands of $P\uparrow$ is almost preserved. As displayed in Fig. 2(f), its CBM locates above the Fermi level, while the VBM lies below the Fermi level, giving rise to a direct band gap of 1.41 eV on the Γ point. As illustrated in Fig. 2(h), the CBM is from the spin-down state of In_2S_3 layer, which mainly comes from In/S-s/p_z orbitals, while for the VBM, it is from the spin-up state of MnSe layer, contributed by Mn-$d_{xy}/d_{x2\text{-}y2}$ and Se-p_x/p_y orbitals. Evidently, the band structure of $P\uparrow$ shows a type-II band alignment. By taking SOC into account, as shown in Fig. 2(g), the degeneracy of the two valence bands at the Γ point is removed and the band gap is reduced to 1.31 eV. Obviously, no band order is inversed in $P\uparrow$ [Fig. 2(h)], suggesting a trivial phase. It is interesting to point out that the relative rotation angle between the two layers might affect the properties of the heterobilayer [38,57].

From above, we can see that upon reversing the electric polarization, the AFM topological phase can be created and annihilated by ferroelectricity in $MnSe/In_2S_3$ heterobilayer. We then investigate the feasibility of ferroelectricity in this heterobilayer using the NEB method. There are two ferroelectric transition paths between $P\downarrow$ and $P\uparrow$; see Figs. S4 [48] and 3(c). For path I with direct shifting of the central S layer, as shown in Fig. S4, the energy barrier against is found to be 0.95 eV per unit cell, which is too large to overcome, while for path II, the transition between $P\downarrow$ and $P\uparrow$ is through a concerted motion of the lower three S-In-S layers, as illustrated in Fig. 3(c). In detail, the transition between $P\downarrow$ and paraelectric state is realized by the left shifting of lower In-S layer and the upper-inclined shifting of inner S layer, and the transition between paraelectric state and $P\uparrow$ phases is caused by the right shifting of lower In-S layer and the

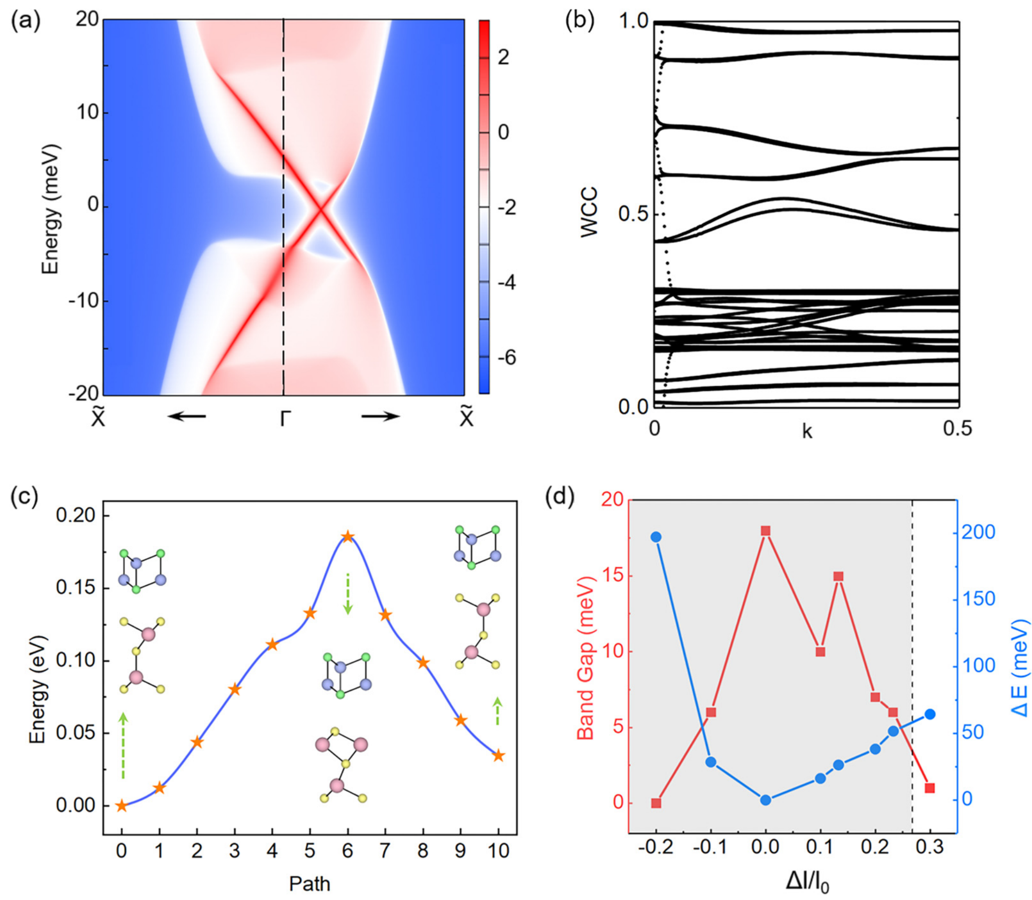

FIG. 3. (a) Topological edge states and (b) evolution of the WCC (b) along k_x for $MnSe/In_2S_3$ heterobilayer under $P\downarrow$. (c) Ferroelectric transition pathway between $P\downarrow$ and $P\uparrow$. (d) Evaluation of total energy increase and band gap with interlayer distance change $\Delta l/l_0$ for $MnSe/In_2S_3$ heterobilayer under $P\downarrow$.

upper-inclined shifting of inner S layer. The energy barrier for the ferroelectric switching from $P\uparrow$ ($P\downarrow$) to $P\downarrow$ ($P\uparrow$) phases is estimated to be 0.151 (0.185) eV per unit cell. These values are significantly smaller than those of Sc_2CO_2 (520 meV/f.u.) and vacancy-doped CrI_3 (650 meV/f.u.), and comparable with those of $VOCl_2$ (180 meV/f.u.) and $CuCrP_2S_6$ (100 meV/f.u.) [58–62], indicating the feasibility of the ferroelectricity in $MnSe/In_2S_3$ heterobilayer. Therefore, the electric-field control of AFM topological physics is achieved in this heterobilayer. It should be noted that some defects would be inevitably formed in the process of synthesizing MnSe [45], which might influence the topological properties of this system, such as changing the Dirac point gap and adjusting the position of the Fermi energy within the gap [54,63,64].

At last, we discuss the influence of layer spacing on the properties of $P\downarrow$. From Fig. 3(d), we can see that the total energy increases, but the band gap shows a decreasing trend, when increasing or decreasing the layer spacing. The increasing of total energy indicates that the interlayer coupling is weakened. Quite naturally, this subsequently would influence the nontrivial band gap of $P\downarrow$. Remarkably, by increasing the interlayer spacing by 30%, the nontrivial band topology even disappears and a transition from nontrivial to trivial phase occurs for $P\downarrow$. On the other hand, with decreasing the layer spacing, the overall net magnetic moment will increase significantly, making the spin splitting of the energy band larger. When the layer spacing is compressed to 80%, the system will show metallicity.

In summary, using first-principles calculations, we map out a design principle for ferroelectric control of AFM topological state by constructing a heterobilayer consisting of an AFM layer of MnSe and a ferroelectric layer of In_2S_3. We find that due to the difference in work function and band gap, the typical type-III band alignment between these two layers can be formed in $MnSe/In_2S_3$ heterobilayer when excluding SOC, which gives rise to two spin-dependent quasi-Dirac cones near the Γ point. When including SOC, a band gap of 18 meV opens at the Dirac cone. This feature implies the nontrivial band topology in $MnSe/In_2S_3$ heterobilayer, which is further demonstrated to be AFM QSH phase. With reversing the electric polarization through ferroelectric switching, the $MnSe/In_2S_3$ heterobilayer becomes semiconducting with a wide band gap, which indicates a nontrivial-to-trivial phase transition. Accordingly, electric-field control of AFM topological physics is achieved in this heterobilayer. Our work opens a direction for the research on FE topology.

This work is supported by the National Natural Science Foundation of China (Grants No. 12274261 and No. 12074217), Shandong Provincial Science Foundation for Excellent Young Scholars (Grant No. ZR2020YQ04),

Shandong Provincial Natural Science Foundation (Grant No. ZR2019QA011), Shandong Provincial Key Research and Development Program (Major Scientific and Technological Innovation Project) (Grant No. 2019JZZY010302), Shandong Provincial QingChuang Technology Support Plan (Grant No. 2021KJ002), and Qilu Young Scholar Program of Shandong University.

The authors declare no competing financial interest.

[1] C. L. Kane and E. J. Mele, Phys. Rev. Lett. **95**, 146802 (2005).
[2] C. L. Kane and E. J. Mele, Phys. Rev. Lett. **95**, 226801 (2005).
[3] K. von Klitzing, G. Dorda, and M. Pepper, Phys. Rev. Lett. **45**, 494 (1980).
[4] D. C. Tsui, H. L. Stormer, and A. C. Gossard, Phys. Rev. Lett. **48**, 1559 (1982).
[5] D. J. Thouless, M. Kohmoto, M. P. Nightingale, and M. den Nijs, Phys. Rev. Lett. **49**, 405 (1982).
[6] K. von Klitzing, Rev. Mod. Phys. **58**, 519 (1986).
[7] M. Z. Hasan and C. L. Kane, Rev. Mod. Phys. **82**, 3045 (2010).
[8] J. Wang, Sci. China Phys. Mech. Astron. **63**, 127031 (2020).
[9] K. He, npj Quantum Mater. **5**, 90 (2020).
[10] B. A. Bernevig, T. L. Hughes, and S. C. Zhang, Science **314**, 1757 (2006).
[11] C. L. Kane L.Fu and E. J. Mele, Phys. Rev. Lett. **98**, 106803 (2007).
[12] Y. L. Chen, J. G. Analytis, J. H. Chu, Z. K. Liu, S. K. Mo, X. L. Qi, H. J. Zhang, D. H. Lu, X. Dai, Z. Fang, S. C. Zhang, I. R. Fisher, Z. Hussain, and Z. X. Shen, Science **325**, 178 (2009).
[13] X. L. Qi and S. C. Zhang, Rev. Mod. Phys. **83**, 1057 (2011).
[14] X.-L. Qi, T. L. Hughes, and S.-C. Zhang, Phys. Rev. B **82**, 184516 (2010).
[15] X. L. Qi, T. L. Hughes, and S. C. Zhang, Phys. Rev. B **78**, 195424 (2008).
[16] L. Zhang, J. Ren, J.-S. Wang, and B. Li, Phys. Rev. B **87**, 144101 (2013).
[17] A. Mook, J. Henk, and I. Mertig, Phys. Rev. B **90**, 024412 (2014).
[18] R. Chisnell, J. S. Helton, D. E. Freedman, D. K. Singh, R. I. Bewley, D. G. Nocera, and Y. S. Lee, Phys. Rev. Lett. **115**, 147201 (2015).
[19] A. Rückriegel, A. Brataas, and R. A. Duine, Phys. Rev. B **97**, 081106(R) (2018).
[20] A. L. Chernyshev and P. A. Maksimov, Phys. Rev. Lett. **117**, 187203 (2016).
[21] R. Matsumoto and S. Murakami, Phys. Rev. Lett. **106**, 197202 (2011).
[22] D. Malz, J. Knolle, and A. Nunnenkamp, Nat. Commun. **10**, 3937 (2019).
[23] J. L. Collins, A. Tadich, W. Wu, L. C. Gomes, J. N. B. Rodrigues, C. Liu, J. Hellerstedt, H. Ryu, S. Tang, S.-K. Mo, S. Adam, S. A. Yang, M. S. Fuhrer, and M. T. Edmonds, Nature (London) **564**, 390 (2018).
[24] R. Resta, Rev. Mod. Phys. **66**, 899 (1994).
[25] R. D. King-Smith and D. Vanderbilt, Phys. Rev. B **47**, 1651(R) (1993).
[26] J. Junquera, M. Zimmer, P. Ordejón, and P. Ghosez, Phys. Rev. B **67**, 155327 (2003).
[27] O. Diéguez, K. M. Rabe, D. Vanderbilt, Phys. Rev. B **72**, 144101 (2005).
[28] M. Sepliarsky, Z. Wu, A. Asthagiri, and R. E. Cohen, Ferroelectrics **301**, 55 (2004).
[29] S. Tinte, M. G. Stachiotti, M. Sepliarsky, R. L. Migoni, and C. O. Rodriguez, J. Phys.: Condens. Matter **11**, 9679 (1999).
[30] G. De Luca, N. Strkalj, S. Manz, M. Fiebig C.Bouillet, and M. Trassin, Nat. Commun. **8**, 1419 (2017).
[31] Z. J. Wang and Y. Bai, Small **15**, 1805088 (2019).
[32] F. Liu, L. You, K. L. Seyler, X. Li, P. Yu, J. Lin, X. Wang, J. Zhou, H. Wang, H. He, S. T. Pantelides, W. Zhou, P. Sharma, X. Xu, P. M. Ajayan, J. Wang, and Z. Liu, Nat. Commun. **7**, 12357 (2016).
[33] K. Chang, J. Liu, H. Lin, N. Wang, K. Zhao, A. Zhang, F. Jin, Y. Zhong, X. Hu, W. Duan, Q. Zhang, L. Fu, Q.-K. Xue, X. Chen, and S.-H. Ji, Science **353**, 274 (2016).
[34] Y. Zhou, D. Wu, Y. Zhu, Y. Cho, Q. He, X. Yang, K. Herrera, Z. Chu, Y. Han, M. C. Downer, H. Peng, and K. Lai, Nano Lett. **17**, 5508 (2017).
[35] C. Cui, W.-J. Hu, X. Yan, C. Addiego, W. Gao, Y. Wang, Z. Wang, L. Li, Y. Cheng, P. Li, X. Zhang, H. N. Alshareef, T. Wu, W. Zhu, X. Pan, and L.-J. Li, Nano Lett. **18**, 1253 (2018).
[36] J. Zhang, D. Zhu, and B. I. Yakobson, Nano Lett. **21**, 785 (2021).
[37] H. Bai, X. Wang, W. Wu, P. He, Z. Xu, S. A. Yang, and Y. Lu, Phys. Rev. B **102**, 235403 (2020).
[38] A. Marrazzo and M. Gibertini, npj 2D Mater. Appl. **6**, 30 (2022).
[39] J. Huang, X. Duan, S. Jeon, Y. Kim, J. Zhou, J. Li, and S. Liu, Mater. Horiz. **9**, 1774 (2022).
[40] G. Kresse and J. Furthmuller, Phys. Rev. B **54**, 11169 (1996).
[41] J. P. Perdew, K. Burke, and M. Ernzerhof, Phys. Rev. Lett. **77**, 3865 (1996).
[42] G. Kresse and D. Joubert, Phys. Rev. B **59**, 1758 (1999).
[43] A. A. Mostofi, J. R. Yates, G. Pizzi, Y.-S. Lee, I. Souza, D. Vanderbilt, and N. Marzari, Comput. Phys. Commun. **185**, 2309 (2014).
[44] S. Grimme, S. Ehrlich, and L. Goerigk, J. Comput. Chem. **32**, 1456 (2011).
[45] S. Guan, C. Liu, Y. Lu, Y. Yao, and S. A. Yang, Phys. Rev. B **97**, 144104 (2018).
[46] J. Neugebauer and M. Scheffler, Phys. Rev. B **46**, 16067 (1992).
[47] M. Aapro, Md. Nurul Huda, J. Karthikeyan, S. Kezilebieke, S. C. Ganguli, H. G. Herrero, X. Huang, P. Liljeroth, and H. Komsa, ACS Nano **15**, 13794 (2021).
[48] See Supplemental Material at http://link.aps.org/supplemental/10.1103/PhysRevB.106.205307 for band structure needed and ferroelectric switching process.
[49] D.-P. Ji, Q. Zhu, and S.-Q. Wang, Surf. Sci. **651**, 137 (2016).
[50] Q. Wang, C. Liu, R. Yao, H. Zhu, X. Liu, M. Wang, Z. Chen, and H. Wang, Comput. Mater. Sci. **172**, 109356 (2020).
[51] G. Lee, Y.-J. Lee, K. Palotás, T. Lee, and A. Soon, J. Phys. Chem. C **124**, 16362 (2020).
[52] Y. Wu, M. K. Y. Chan, and G. Ceder, Phys. Rev. B **83**, 235301 (2011).

[53] A. Goyal, P. Gorai, E. S. Toberer,, and V. Stevanović, npj Comput. Mater. **3**, 42 (2017).
[54] T. Das, X. Rocquefelte, and S. Jobic, J. Phys. Chem. C **124**, 19426 (2020).
[55] C.-X. Liu, R.-X. Zhang, and B. K. VanLeeuwen, Phys. Rev. B **90**, 085304 (2014).
[56] N. Mao, H. Wang, X. Hu, C. Niu, B. Huang, and Y. Dai, Phys. Rev. B **102**, 115412 (2020).
[57] Z.-D. Song and B. A. Bernevig, Phys. Rev. Lett. **129**, 047601 (2022).
[58] H. Ai, X. Song, S. Qi, W. Li, and M. Zhao, Nanoscale **11**, 1103 (2019).
[59] A. Chandrasekaran, A. Mishra, and A. Singh, Nano Lett. **17**, 3290 (2017).
[60] Y. Zhao, L. Lin, Q. Zhou, Y. Li, S. Yuan, Q. Chen, S. Dong, and J. Wang, Nano Lett. **18**, 2943 (2018).
[61] Y. Ren, S. Dong, and M. Wu, ACS Appl. Mater. Interfaces **10**, 35361 (2018).
[62] J. Qi, H. Wang, X. Chen, and X. Qian, Appl. Phys. Lett. **113**, 043102 (2018).
[63] M. Garnica, M. M. Otrokov, P. Casado Aguilar, I. I. Klimovskikh, D. Estyunin, Z. S. Aliev, I. R. Amiraslanov, N. A. Abdullayev, V. N. Zverev, M. B. Babanly, N. T. Mamedov, A. M. Shikin, A. Arnau, A. L. Vázquez de Parga, E. V. Chulkov, and R. Miranda, npj Quantum Mater. **7**, 7 (2022).
[64] Z. Huang, M.-H. Du, J. Yan, and W. Wu, Phys. Rev. Mater. **4**, 121202(R) (2020).